Electric and magnetic terahertz nonlinearities resolved on the sub-cycle scale

2013 New J. Phys. 15 065003

(http://iopscience.iop.org/1367-2630/15/6/065003)

New Journal of Physics
The open access journal for physics

Electric and magnetic terahertz nonlinearities resolved on the sub-cycle scale

Alexej Pashkin[1], **Alexander Sell**[1], **Tobias Kampfrath**[2]
and Rupert Huber[3,4]
[1] Department of Physics and Center for Applied Photonics, University of Konstanz, Universitätsstraße 10, 78464 Konstanz, Germany
[2] Department of Physical Chemistry, Fritz Haber Institute of the Max Planck Society, Faradayweg 4-6, 14195 Berlin, Germany
[3] Department of Physics, University of Regensburg, Universitätsstraße 31, 93053 Regensburg, Germany
E-mail: rupert.huber@physik.uni-regensburg.de

New Journal of Physics **15** (2013) 065003 (18pp)
Received 8 March 2013
Published 3 June 2013
Online at http://www.njp.org/
doi:10.1088/1367-2630/15/6/065003

Abstract. Table-top sources of intense multi-terahertz (THz) pulses have opened the door to studies of extreme nonlinearities in the previously elusive mid- to far-infrared spectral regime. We discuss two concepts of fully coherent coupling of phase-locked THz pulses with condensed matter. The first approach demonstrates two-dimensional multi-THz spectroscopy of the semiconductor material InSb. By phase- and amplitude-sensitive detection of the nonlinear optical response, we are able to separate incoherent pump–probe signals from coherent four-wave mixing and reveal extremely non-perturbative nonlinearities. While this class of interactions is mediated by the electric field component of the THz pulse, the second approach is complementary, as it demonstrates that, alternatively, the magnetic THz field may be exploited to selectively control the spin degree of freedom in antiferromagnetic NiO.

---

[4] Author to whom any correspondence should be addressed.

Contents

1. Introduction

The incentive to study and control low-energy collective excitations in condensed matter on the femtosecond time scale has spurred on the development of a unique arsenal of sources and detectors in the terahertz (THz) spectral band [1, 2]. Inherently phase-locked single-cycle THz pulses have become routinely available while ultrabroadband electro-optic sensors trace the transient field with respect to absolute phase and amplitude throughout the entire far- and mid-infrared range [3, 4]. Low-energy dynamics have thus become amenable to observation on time scales shorter than a single oscillation period of light [5].

The crucial step from ultrafast linear to ultrafast nonlinear THz interactions has been heralded by the recent boost in energies of THz pulses beyond $1\,\mu$J, whereby peak electric fields above $1\,\mathrm{MV\,cm^{-1}}$ have been reached [6–10]. When intense THz electromagnetic pulses interact with the many-body system of a solid, a variety of non-equilibrium scenarios may result. Recent experiments have explored intervalley scattering [11–13], interband tunneling [14], impact ionization [15, 16], and the anisotropy of the effective mass [17] in semiconductors, anharmonicities of a soft phonon mode in ferroelectrics [18], as well as non-thermal suppression of electronic localization in strongly correlated systems [19, 20]. Most studies have concentrated on the effects of THz excitation after the coherence between the external driving field and the induced polarization has decayed. On the other hand, first examples of coherent THz nonlinearities have been demonstrated with semiconductors [21–24] and rotational states of gas molecules [25, 26]. These studies re-emphasize the importance of dynamics occurring on timescales shorter than the dephasing time of the electron system. Here we report on two novel classes of coherent nonlinearities. The recent breakthrough in the generation of ultra-intense multi-THz transients with peak electric fields up to $100\,\mathrm{MV\,cm^{-1}}$ [27, 28] allows us to explore a regime of a light–matter interaction where the Rabi frequency becomes comparable to the oscillation frequency of the driving THz field. In this case, the nonlinear response reaches

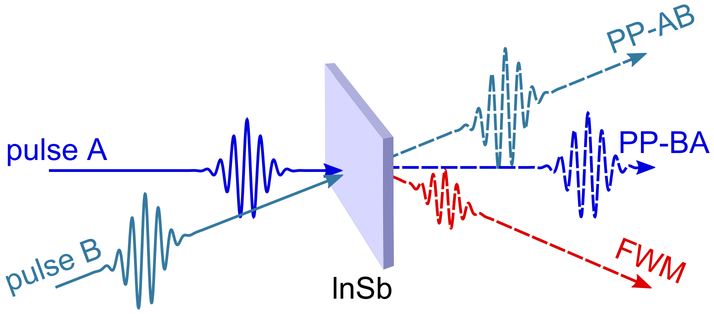

Figure 1. Schematic representation of a non-collinear FWM experiment: two high-field THz pulses are focused into an InSb sample. The dashed lines illustrate the generated nonlinear signals. The pump–probe signals PP-BA (pump B/ probe A) and PP-AB (pump A/probe B) propagate in the same direction as the probe pulses A and B, respectively. The coherent FWM signal depends on the relative phase of the interacting pulses and propagates in a different direction.

the limit of extremely non-perturbative optics [29]. Furthermore, the complementary magnetic component of THz pulses can strongly couple to a spin subsystem and coherently control the precession of a macroscopic magnetization [30, 31]. Both aspects are covered in our discussion.

In the first part of this article, we report on the coherent nonlinear THz response of an interband polarization in the narrowband semiconductor InSb, studied by means of field-resolved four-wave mixing (FWM) spectroscopy [32]. The carrier frequency of the THz driving field is set well below the interband resonance. In the limit of perturbative light–matter interactions, as are considered in classical nonlinear optics, the FWM process is fully governed by a third-order optical nonlinearity. However, this regime is realized only when the Rabi frequency is much smaller than the detuning of the driving frequency from a resonance. Our experiment demonstrates that this condition is violated for peak electric fields in excess of $3\,\mathrm{MV\,cm^{-1}}$, as the FWM signal shows clear signatures of a non-perturbative response caused by coherent Rabi flopping.

The second part of this article focuses on an ultrafast control of collective spin precession in antiferromagnetic NiO at frequencies as high as 1 THz [33]. By using intense magnetic THz transients, we switch a coherent magnon on and off, with sub-cycle precision.

2. Non-perturbative nonlinear response of a bulk semiconductor under off-resonant terahertz (THz) excitation

Semiconductors, due to our advanced theoretical understanding and experimental control of their material properties, provide a prime test bed for the investigation of light–matter coupling in quantum many-body systems. In particular, their interaction with extremely intense THz electromagnetic fields has attracted attention for potential applications in both modern optics and high-speed optoelectronics [11, 12, 14, 16, 17, 34]. We utilize high-field multi-THz pulses to study the coherent response of bulk InSb by means of two-dimensional spectroscopy. Following the generic concept of a degenerate FWM experiment we address an interaction of two intensive THz pulses within a sample, as illustrated schematically in figure 1. The temporal position of pulse A is fixed while pulse B is delayed with respect to the former by a variable delay time τ.

The leading pulse (A or B, depending on the sign of τ) can induce a change in the optical constants of the sample and, thus, affect the propagation of the subsequent pulse. This process gives rise to a nonlinear pump–probe signal which gradually varies as a function of τ. The pump–probe signal temporally coincides with the probe pulse and propagates in the same spatial direction. An alternative interaction pathway that is also possible proceeds as follows: a coherent polarization induced by the leading pulse can interfere with a trailing pulse, resulting in a periodic modulation of the optical constants. Part of the second pulse may then diffract from the emergent transient grating, generating a FWM signal. In the case of the non-collinear geometry shown in figure 1, the FWM signal propagates in a different direction than either pulses A or B, where the direction is defined by the conservation of the wavevectors involved in the nonlinear interaction. As we will demonstrate below, FWM and pump–probe signals may also be distinguished directly via the dependence of their respective phases. Complete amplitude and phase resolution of the nonlinear optical response will provide us with a sensitive tool to separate various nonlinearities and do so independently of their spatial propagation direction.

2.1. Field-sensitive two-dimensional spectroscopy

In order to test the validity of these considerations we explore the FWM response of a bulk sample of the semiconductor InSb. This material features a narrow direct bandgap of $E_{\mathrm{g}} = 170\,\mathrm{meV} \mathrel{\hat{=}} 41.1\,\mathrm{THz}$. A single crystalline window with a thickness of $30\,\mu$m is investigated at room temperature. The small energy gap of InSb results in a relatively large density of intrinsic charge carriers of $n_0 = 2 \times 10^{16}\,\mathrm{cm}^{-3}$. High-field THz pulses are generated by a table-top laser system using difference frequency mixing in a GaSe emitter [28]. The duration of the pulses amounts to 150 fs (full-width at half-maximum (FWHM)) and their carrier frequency is $f_0 = 23\,\mathrm{THz}$. Thus, the complete spectrum is located below the absorption edge of InSb, ensuring off-resonant driving of the polarization response. The THz radiation is tightly focused onto the surface of the semiconductor. The electric fields re-emitted by the oscillating polarization in the sample are collected by an off-axis parabolic mirror with large numerical aperture ensuring the angle-integrated detection. The field-resolved THz waveforms are measured electro-optically in a GaSe sensor. Further technical details of the experiment are summarized in [32].

The total field emitted from InSb, in the presence of both pulses A and B, is measured as a function of the electro-optic sampling delay time t and the relative pulse delay τ (see figure 2(a)). The peak electric fields at the focal spot, which has a diameter (FWHM) of $85\,\mu$m, amount to $2\,\mathrm{MV\,cm}^{-1}$ per pulse. This value corresponds to an intensity of $\approx 10.6\,\mathrm{GW\,cm}^{-2}$. The nonlinear contribution is obtained by subtracting the transmitted fields of the individual pulses A and B from the total electric field. The resulting two-time-dependent nonlinear response is shown in figure 2(b).

Even though these data contain all nonlinear optical processes in an angularly integrated way, the FWM signals may be sharply discriminated from the pump–probe signatures by their specific phase dependencies. Since the FWM process relies on the interference of both driving pulses, a FWM signal depends on the relative phase of both excitation fields and, therefore, the phase periodically varies as a function of τ. A Fourier transformation in two-dimensional frequency space allows us to separate FWM from pump–probe nonlinear processes. Figure 2(c) depicts the amplitude spectrum of the total nonlinear signal in frequency space. Different contributions to the nonlinear signal appear as distinct pairs of maxima conjugated by the inversion operation with respect to the origin [35].

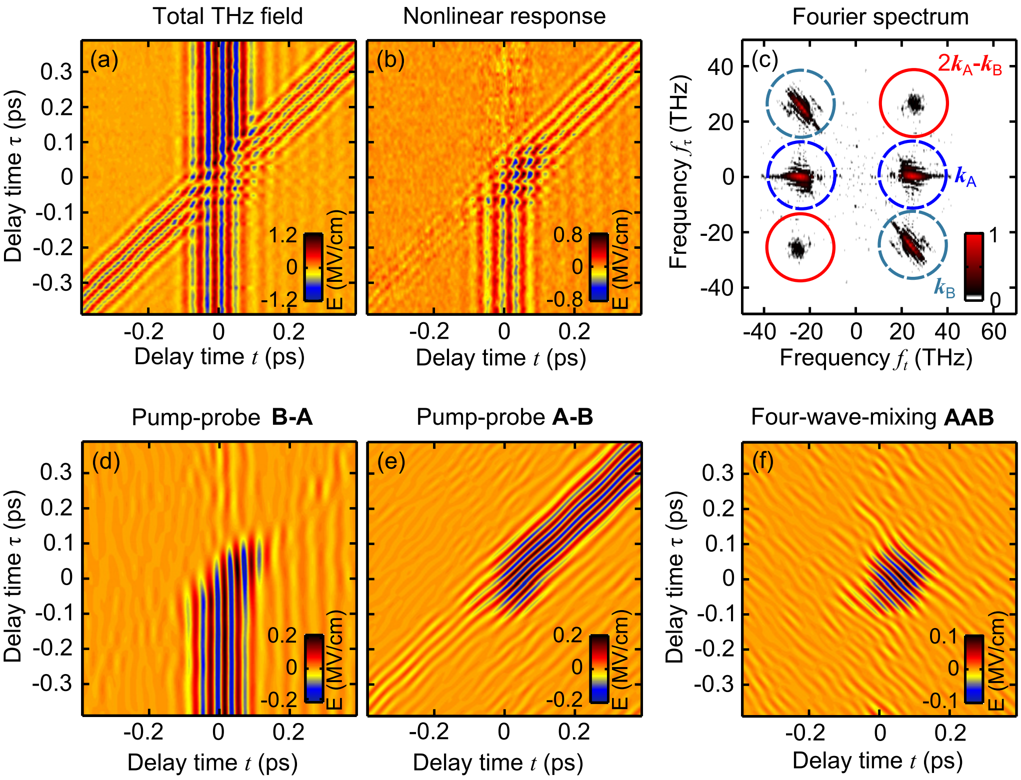

Figure 2. (a) Total electric field of the two THz transients transmitted through InSb plotted as a function of sampling delay time t and temporal offset τ between the transients. (b) Nonlinear contribution E_{NL} to the total electric field. (c) Two-dimensional Fourier spectrum of E_{NL} with pump–probe and FWM contributions located at different points of the frequency plane. (d, e) Time-domain pump–probe signals PP-BA and PP-AB obtained by inverse FT of the signals at $\boldsymbol{k}_{\mathrm{A}}$ and $\boldsymbol{k}_{\mathrm{B}}$, respectively. (f) Time-domain FWM signal obtained by inverse FT of the signal at $2\boldsymbol{k}_{\mathrm{A}} - \boldsymbol{k}_{\mathrm{B}}$.

For a qualitative understanding of the origin of the various maxima in frequency space, it is instructive to note that the Fourier transform (FT) of pulse A would be centered at the position $\boldsymbol{k}_{\mathrm{A}} = (f_0, 0)$ and its conjugate $-\boldsymbol{k}_{\mathrm{A}}$. This fact is straightforward to understand since the electric field of pulse A, which is not shifted in time, does not oscillate as a function of τ, while it does oscillate with frequency f_0 along time t. As a consequence of this, nonlinear signals observed at $\boldsymbol{k}_{\mathrm{A}}$ represent changes in pulse A induced by pulse B. In other words, these signatures represent pump–probe signals with pulses B and A acting as pump and probe, respectively. As a shorthand we denote this interaction as PP-BA. The temporal evolution of this particular signal is obtained by the selective inverse FT of the signal at $\boldsymbol{k}_{\mathrm{A}}$ (see figure 2(d)). Due to causality, the signature PP-BA gradually vanishes for $\tau > 0$ when the pulse B arrives after the probe pulse A.

Similarly, the spot located at $\boldsymbol{k}_{\mathrm{B}} = (+f_0, -f_0)$ corresponds to changes imprinted on pulse B. The temporal shift of pulse B leads to oscillations of its electric field along the τ-axis resulting in $f_\tau = -f_0$. The negative sign of the frequency is caused by the positive phase shift in the field profile when the delay time t increases. The corresponding pump–probe signal PP-AB appears for $\tau > 0$ when the time order of the pulses is reversed (see figure 2(e)).

Finally, the maximum at the position $2\boldsymbol{k}_{\mathrm{A}} - \boldsymbol{k}_{\mathrm{B}} = (+f_0, +f_0)$ and its conjugate correspond to a coherent FWM signal. As pointed out above, the FWM field also oscillates as a function of τ due to the phase-sensitive character of the interaction between the pulses A and B. However, in contrast to the PP-AB signal, the FWM signature appears at positive frequency $f_\tau = f_0$. Therefore, its phase experiences a negative shift with increasing delay time t, as it is seen in the time-domain of the FWM signal shown in figure 2(f).

In contrast to the FWM signal, the pump–probe signals observed in our experiment are temporally extended far beyond the duration of the interacting THz pulses themselves. This observation indicates that the main contribution to the pump–probe response in InSb originates from a long-living electron–hole plasma produced by the intense THz field of the pump pulse. Possible mechanisms of free carrier generation by an excitation below the bandgap of InSb such as impact ionization [15], two-photon absorption (TPA) [36] or interband tunneling [37] have been studied previously. Here we concentrate on the FWM signal, which characterizes coherence induced in the sample by the phase-stable THz pulses.

2.2. *From perturbative to non-perturbative four-wave mixing (FWM)*

Figures 3(a)–(c) show the time-domain FWM obtained from measurements performed with peak electric fields of 2, 3.5 and 5.3 MV cm^{-1} per pulse, respectively. The envelope of the FWM signal qualitatively changes with increasing field strength and evolves from an oval shape at the lowest field (figure 3(a)) via an S-shape at 3.5 MV cm^{-1} (figure 3(b)) towards a split area at the highest excitation intensity (figure 3(c)). This splitting results in a minimum of the FWM signal along the diagonal of the time window ($t = \tau$) where the total excitation field reaches maximal values. In the following discussion we demonstrate that this behavior is an unambiguous signature of a non-perturbative polarization response in InSb.

In order to understand the character of the light–matter interaction in our experiment, we perform simulations of the FWM response assuming either a perturbative response due to a third-order nonlinearity $\chi^{(3)}$ or a response of a quantum two-level system coherently driven by intense THz pulses. In both frameworks, the electric fields of the THz pulses are given by

$$E(z,t) = \sqrt{I(z,t-\tau)Z}\,\exp[\mathrm{i}\Theta(z,t)]\exp[-\mathrm{i}kz + \mathrm{i}\omega_0(t-\tau)], \tag{1}$$

where z is the spatial coordinate along the beam axis, $I(z,t)$ is the Gaussian intensity envelope with a FWHM duration of 100 fs, $Z = \sqrt{\mu_0/\varepsilon_0\varepsilon}$ is the wave impedance, k and $\omega_0 = 2\pi f_0$ are the wavevector and the carrier frequency, and $\Theta(z,t)$ is the phase shift, which is initially set to zero (Fourier-limited pulses).

2.3. *Theory of perturbative FWM*

The pulse propagation through the sample affected by $\chi^{(3)}$ nonlinearities and free charge carriers can be described by the following system of equations [37]:

$$\frac{\partial I(z,t)}{\partial z} = -\alpha I(z,t) - \beta I^2(z,t), \tag{2}$$

$$\frac{\partial \Theta(z,t)}{\partial z} = -A\Delta n(z,t) + BI(z,t), \tag{3}$$

$$\frac{\partial \Delta n(z,t)}{\partial t} = \frac{\beta I^2(z,t)}{2\hbar\omega_0}, \tag{4}$$

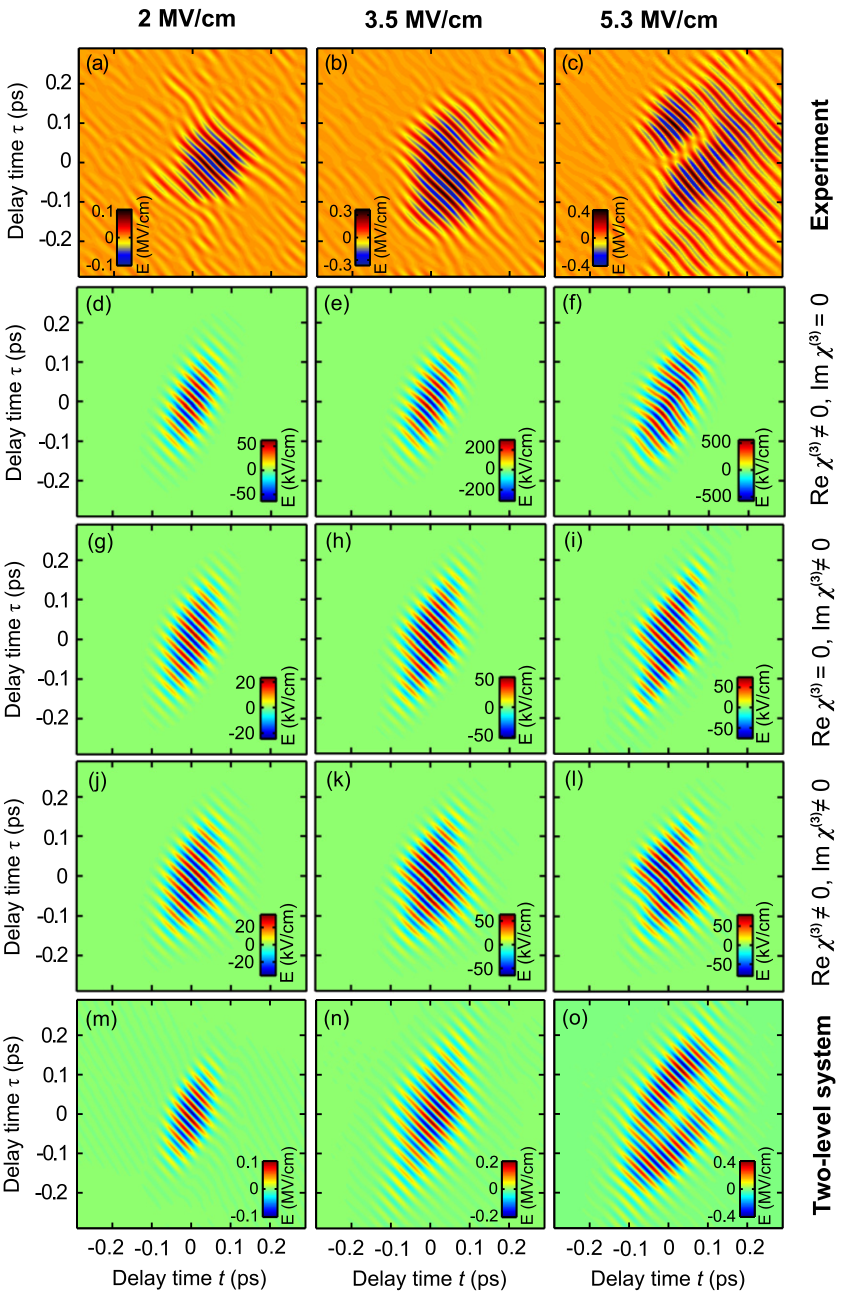

Figure 3. Experimental FWM signals generated by THz transients with peak electric fields of (a) 2 MV cm^{-1}, (b) 3.5 MV cm^{-1} and (c) 5.3 MV cm^{-1}. Calculated FWM signals for the same driving fields using models which take into account (d)–(f) only the real part of $\chi^{(3)}$ (Kerr effect), (g)–(i) only the imaginary part of $\chi^{(3)}$ (TPA), (j)–(l) the real and imaginary parts of $\chi^{(3)}$ and the contribution of the field-induced electron–hole plasma, (m)–(o) coherent excitation of a quantum two-level system.

Here β is the TPA coefficient and Δn is the excess density of free carriers generated via TPA. The coefficient $\alpha = \sigma_{\mathrm{FC}}(n_0 + \Delta n)$ describes the linear absorption due to the holes in the valence band, where $\sigma_{\mathrm{FC}} = 5.6 \times 10^{-16}\,\mathrm{cm}^2$ is the interaction cross-section [37]. The TPA coefficient β

is directly proportional to the imaginary part of the third-order nonlinear coefficient, Im $\chi^{(3)}$. In turn, the real part Re $\chi^{(3)}$ is responsible for the Kerr effect, which leads to the phase modulation described by the second term on the right-hand side of equation (3). The first term in this equation takes into account the phase modulation caused by the plasma response of free carriers in the sample. The respective coefficients for InSb are $A = 1.15 \times 10^{-24}\,\mathrm{m}^{-4}$ [37] and $B = 1.7 \times 10^{-19}\,\mathrm{m\,W}$ [38]. Here the main contribution to the Kerr effect stems from the response of free electrons in the non-parabolic conduction band of InSb [38], which exceeds the nonlinear response of the bound valence-band electrons by more than an order of magnitude. The TPA coefficient β is set to be 0.3 cm MW in order to obtain the closest agreement with the experimental results. This value is somewhat smaller than the 2 cm MW^{-1} typically reported by studies that use picosecond and femtosecond pulses with peak intensities of several MW cm^{-2} [36, 37]. The discrepancy between the two coefficients may indicate a saturation of the TPA process by Pauli blocking, as our experiment was performed using GW cm^{-2} peak intensities. Eventually, the TPA picture may break down due to the onset of a non-perturbative excitation regime.

Our simulations based on equations (2)–(4) assume plane wave propagation and, thus, neglect self-focusing effects which are assumed to be minor in the cases of the 30 μm-thick sample and the apertureless electro-optic detection utilized in our experiment. In order to analyze the FWM response produced by perturbative nonlinear effects we introduce them step by step in our simulations. Let us first consider only the Kerr effect related to the Re $\chi^{(3)}$ nonlinearity and neglect all other contributions ($B \neq 0, \alpha = \beta = 0$). The simulated time-domain FWM signals are shown in figures 3(d)–(f) for the same peak THz fields as those used in the experiment. The envelope of the FWM signature remains oval for all excitation intensities with a noticeable distortion of the constant phase lines due to a strong cross-phase modulation at the highest peak field of 5.3 MV cm^{-1}. Thus, the pure Kerr effect cannot explain the experimental observations, even though the amplitudes of the simulated FWM signals are comparable to the experimental values.

As a second step, we present the results of simulations that take into account solely the pulse attenuation by the TPA process (only equation (2) where $\beta \neq 0$ and $\alpha = 0$). At the lowest field setting, TPA causes an oval-shaped FWM signal, as shown in figure 3(g). Higher driving fields lead to the characteristic S-shaped FWM signals shown in figures 3(h) and (i). The shape of these signals resembles the experimentally observed signatures for peak fields of 3.5 MV cm^{-1} (figure 3(b)). However, TPA simulations for even higher driving fields (not shown) result in the same S-shaped FWM signatures and do not show any sign of the splitting observed in the experiment. Moreover, the amplitude of the simulated FWM signals saturates at a level of $\approx$50 kV cm^{-1} and stays far below the amplitudes observed in the experiment (see figures 3(h) and (i)). This fact can be qualitatively understood by keeping in mind that the TPA is proportional to the radiation intensity: during propagation the intensity of the pulses is mostly suppressed in the middle of the pulse, where the intensity is highest. Therefore, the intensity profile of the pulses develops a 'flat' top and the nonlinear signal saturates. Obviously, the TPA process cannot account for the field minimum observed in the center of the FWM signal (figure 3(c)).

In fact, the switch-off analysis presented above is not completely physical. TPA has to be considered since $2\hbar\omega_0 > E_\mathrm{g}$, while the Kramers–Kronig relations enforce the simultaneous presence of Re $\chi^{(3)}$ [39]. Moreover, the dominating contribution of the free carriers to the phase modulation and the energy absorption also must be taken into account. The results of such simulations are shown in figures 3(j)–(l). The shapes and amplitudes of the modeled FWM signals are similar to those shown in figures 3(g)–(i). Thus, we conclude that TPA dominates the simulated perturbative response. A strong nonlinear absorption makes the role of the Kerr effect almost negligible and the nonlinearity of the free carrier plasma leads to a broadening of the FWM signature along the time axis t and a partial compression along the τ-axis. In any case, our model demonstrates that neither the shape nor the amplitude of the experimental FWM signals are adequately described within the framework of perturbative nonlinear optics.

2.4. Non-perturbative FWM in the two-level approximation

We now proceed by demonstrating that these deficiencies may be cured with numerical simulations of our FWM experiment using a simplified model of a two-level system, which represents the interband resonance in InSb. The pulse propagation is modeled by the Maxwell–Bloch equations [40]. Based on previous reports, we assume a dephasing time $T_2 = 1\,\mathrm{ps}$ [41]. Since the timescales involved in our FWM experiment are much shorter than T_2, the exact values of the relaxation time hardly affect the results of the simulations. For the same reasons we choose a depopulation time $T_1 = 10\,\mathrm{ps}$. The remaining two parameters of the model, i.e. the transition dipole moment $\mu_{12} = 2.4\,e\mathrm{\AA}$ and the density of the two-level systems $N = 2.9 \times 10^{20}\,\mathrm{cm}^{-3}$ are adapted to provide best agreement with the experimental data. The simulated FWM signals are depicted in figures 3(m)–(o). Remarkably, these simulations reproduce all essential features observed in the experiment, such as the amplitudes of the FWM signals and, even more importantly, the characteristic splitting for the peak field of $5.3\,\mathrm{MV\,cm}^{-1}$. This clearly demonstrates the non-perturbative character of the polarization response in InSb, in spite of the strong detuning of the excitation with respect to the interband resonance.

Better physical insight can be gained by examining the simulated coherent polarization dynamics of the interband resonances in InSb driven by pulses A and B at vanishing delay time τ. Our simulations assume an ensemble of 50 two-level systems with resonance frequencies distributed between 41 THz and 51 THz with an energy density proportional to $\sqrt{\hbar\omega - E_g}$, coarsely mimicking the continuum of interband transitions. Figure 4(a) shows the normalized temporal profiles of the driving THz pulses with peak fields of $2\,\mathrm{MV\,cm}^{-1}$ per pulse ($4\,\mathrm{MV\,cm}^{-1}$ in total), the total polarization, and the frequency components of the polarization centered around the fundamental frequency f_0, as obtained by Fourier filtering shown in figure 2(c). As one can see in figure 4(a), the total polarization P_{tot} as well as its fundamental component P_{fund} closely follow the driving electric field E_{THz}. Thus, small deviations of P_{tot} from E_{THz} can be described within a perturbative approach. Correspondingly, the simulated FWM signal has an oval shape (figure 3(m)). The situation changes when the peak driving fields reach $3.5\,\mathrm{MV\,cm}^{-1}$ per pulse. Figure 4(b) demonstrates that the total polarization oscillates at much higher frequencies after the driving field has assumed its maximum, i.e. at delay times $t > 0$. For such excitation conditions, the Rabi frequency $\Omega_R \propto \mu_{12} E_{\mathrm{THz}}$ characterizing the strength of light–matter interactions becomes comparable to the detuning of the fundamental frequency from the lowest interband resonances. This leads to a non-perturbative response of the two-level systems driven into the regime of carrier-wave Rabi flopping [32, 42]. The major contribution to P_{tot} occurs at higher odd harmonics [43, 44], whereas P_{fund} starts to decrease (see figure 4(b)). At the highest peak driving fields of $5.3\,\mathrm{MV\,cm}^{-1}$ this effect becomes very pronounced and a distinct minimum

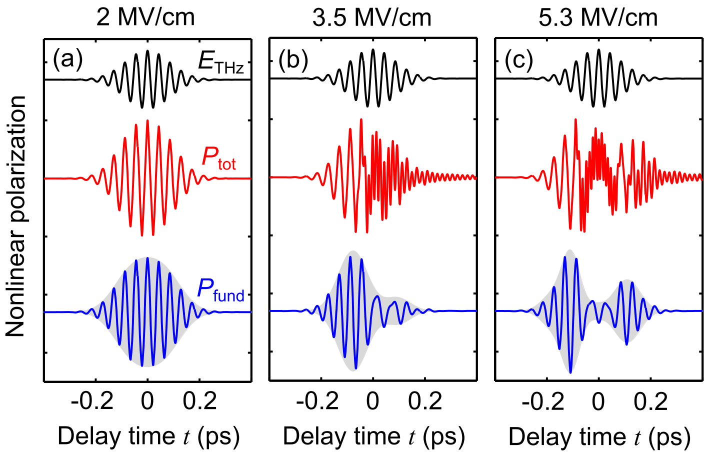

Figure 4. Non-perturbative polarization response of an ensemble of two-level systems simulated for excitation of temporally overlapping THz transients ($\tau = 0$) with peak electric fields of (a) $2\,\mathrm{MV\,cm^{-1}}$, (b) $3.5\,\mathrm{MV\,cm^{-1}}$ and (c) $5.3\,\mathrm{MV\,cm^{-1}}$. Black lines correspond to the normalized driving field. The time evolution of the total polarization P_{tot} and the part of P_{tot} oscillating at the fundamental frequency of the driving field P_{fund} are shown by red and blue lines, respectively.

develops in the center of P_{fund}, as shown in figure 4(c). Notably, this effect is responsible for the splitting of the time-domain FWM signal observed in our experiment (figure 3(c)). Thus, we establish an unequivocal manifestation of a non-perturbative response of InSb under an off-resonant excitation by high-field THz pulses.

3. Spin control in antiferromagnets using magnetic THz transients

In the preceding section, the transient electric field $\boldsymbol{E}$ of intense THz pulses was employed to coherently drive matter into a non-equilibrium state. The magnetic field component $\boldsymbol{B}$ was ignored since it exerts a force (the Lorentz force) on an electron that is smaller by a factor of $|\boldsymbol{v}|/c$ than the electric contribution (the Coulomb force). Here, $\boldsymbol{v}$ is the electron velocity, and in atoms or molecules, $|\boldsymbol{v}|/c$ is of the order of the fine-structure constant of $\approx 1/137$. Similar arguments indicate that the interaction energy between the $\boldsymbol{B}$-field and its induced magnetic dipole is reduced by a factor of $(\boldsymbol{v}/c)^2 \sim 10^{-4}$ compared to the interaction energy between $\boldsymbol{E}$ and its induced electric dipole [45].

On the other hand, magnetic fields represent the most direct handle to control the quantum-mechanical spin $\boldsymbol{S}$ of an electron. As $\boldsymbol{S}$ is associated with a magnetic dipole moment it couples to $\boldsymbol{B}$ through the Zeeman Hamiltonian $\gamma \boldsymbol{S} \cdot \boldsymbol{B}$ where γ denotes the gyromagnetic constant. As a consequence, a perturbing magnetic field exerts a torque $\gamma \boldsymbol{S} \times \boldsymbol{B}$, thereby pulling the spin out of its equilibrium direction, set by an effective internal magnetic field $\boldsymbol{B}_{\mathrm{int}}$ (figure 5(a)). Note that the weak Zeeman torque is resonantly enhanced when the driving frequency equals $\gamma \boldsymbol{B}_{\mathrm{int}}$. In ferromagnets, this so-called Larmor frequency does not exceed 10 GHz, in contrast to antiferromagnets in which the perturbing field destroys the perfectly antiparallel spin

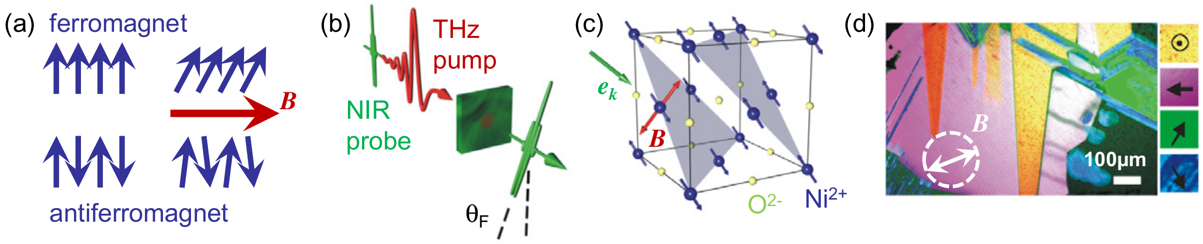

Figure 5. (a) Schematic illustrating the very different response of ferromagnets and antiferromagnets to an external magnetic field $\boldsymbol{B}$. (b) THz-pump magnetooptic-probe scheme. (c) Lattice geometry of NiO along with the incident THz magnetic field pulse. (d) Polarization micrograph of the NiO sample studied. Arrows indicate the four T-domain types and the circle indicates the excited volume.

configuration (figure 5(a)). Thus, the exchange interaction becomes operative and induces a strong repulsive torque, thereby pushing the resonance frequency of long-wavelength spin waves into the THz range. These high frequencies make antiferromagnets, which represent the majority of magnetically ordered solids in nature, particularly interesting for high-speed spin manipulation.

So far, direct Zeeman-type control of magnons has been demonstrated in ferromagnets on time scales of ~100 ps [46–48], yet it has been inhibited in antiferromagnets due to a lack of sufficiently fast and intense magnets. Instead, optical pulses have been used to generate effective transient magnetic fields either through heating or stimulated Raman processes [49]. Ultrafast electron heating leads to a rapid change in the internal field $\boldsymbol{B}_{\mathrm{int}}$, yet the associated cooling dynamics limit the speed and thus the compatibility of electron heating with coherent control of THz resonances. The non-thermal Raman approach invokes the electric field of an off-resonant laser pulse but requires materials with massive spin–orbit coupling. In addition, the underlying microscopic processes of both optical approaches are not yet fully understood [49] and lack the simplicity and universality of the generic Zeeman-type control.

Here, we exploit the recent development of sources of high-field phase-locked electromagnetic transients with amplitudes of $\sim 1\,\mathrm{MV\,cm^{-1}}$ and ~0.5 T that cover the frequency range below 10 THz [6, 8–10, 17]. Using such pulses, we switch a coherent 1-THz magnon oscillation in antiferromagnetic NiO on and off on a single-cycle timescale.

3.1. Experimental details

A schematic of our experiment is shown in figure 5(b): an intense THz magnetic field transient incident on the sample system is expected to perturb the electron spins via direct Zeeman interaction. The induced magnetization $\boldsymbol{M}(t)$ is probed by a near-infrared laser pulse as a function of the delay time t after the THz pump. Here, we take advantage of the Faraday effect: the projection of the magnetization onto the propagation direction $\boldsymbol{e}_k$ of the probe pulse causes a transient circular birefringence which rotates the probe polarization by an angle [49]

$$\theta_{\mathrm{F}}(t) = Vd\langle \boldsymbol{e}_k \cdot \boldsymbol{M}\rangle. \tag{5}$$

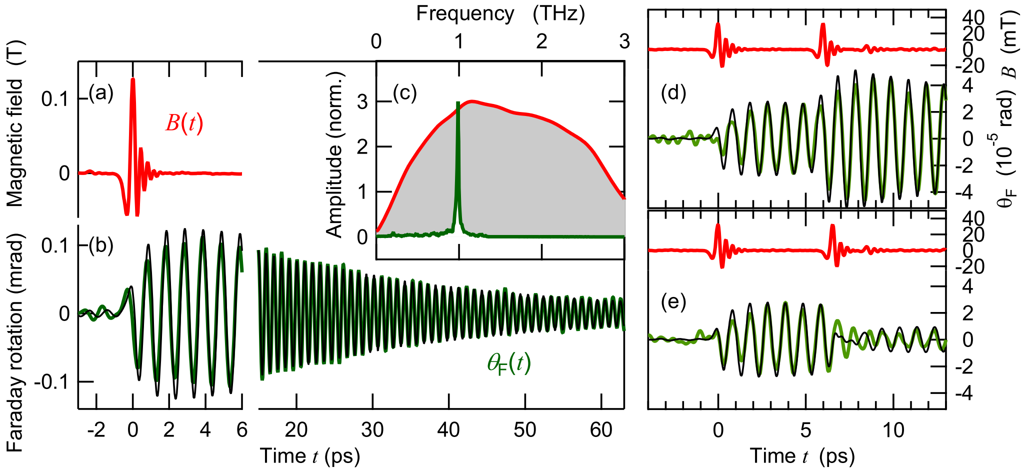

Figure 6. Coherent control of THz spin precession using various magnetic-field transients. (a) Magnetic field of an incident single pulse $B(t)$ and its (b) induced Faraday rotation $\theta_{\mathrm{F}}(t)$ as a function of pump–probe delay t. (c) Fourier amplitude spectrum of B and θ_{F}. (d) Double-pulse excitation with the second pulse in or (e) out of phase with the spin precession triggered by the first pulse. Thin solid lines in θ_{F}-plots represent simulation results (amplitude scaled by a factor of 0.7).

Here, V and d are the magneto-optic Verdet constant and the sample thickness, respectively, whereas $\langle . \rangle$ denotes averaging over the probed sample volume.

We choose the textbook antiferromagnet NiO as a test system for this study. The high Néel temperature $T_{\mathrm{N}} = 523\,\mathrm{K}$ allows us to conduct all experiments under ambient conditions. Figure 5(c) shows the quasi-cubic crystal structure. Below T_{N}, the Ni^{2+} spins are ordered ferromagnetically within $\{111\}$ planes where they point along the $\langle 11\bar{2} \rangle$-axis [50]. Adjacent planes are oppositely magnetized due to antiferromagnetic coupling. Each of the four equivalent $\langle 111 \rangle$ stacking directions defines a twin (T) domain which is subdivided into spin-rotation (S) domains as the spins can point in three equivalent in-plane directions. Birefringence induced by a slight lattice contraction along the stacking axes allows us to map the domain structure with a polarization-sensitive microscope as seen in figure 5(d). For our free-standing NiO window (thickness $d = 45\,\mu\mathrm{m}$), we find dimensions of the T domains of the order of $100\,\mu\mathrm{m}$. The S domains are not resolved since they are less than $1\,\mu\mathrm{m}$ wide [50]. Inelastic neutron and light scattering as well as infrared absorption have identified long-wavelength antiferromagnetic magnon modes in NiO at ≈ 0.2 and 1 THz [51].

A high-field THz transient is generated by optical rectification of 5-mJ, 800-nm, 100-fs laser pulses in a large-area ZnTe emitter and focused onto a single T domain (white circle in figure 5(d)). The microscopic geometry depicted in figure 5(c) precisely corresponds to the experimental situation for one of the three possible S domains. Figure 6(a) shows the time trace $B(t)$ of the incident magnetic pulse in its polarization plane as recorded by electro-optic sampling [17]. This single-cycle transient reaches a magnetic peak field of 0.13 T and covers a broad spectral range from 0.1 to 3 THz, fully overlapping the magnon resonance at 1 THz (figure 6(c)). An 8-fs pulse with a central photon energy of 1 eV serves as our probe to map out the pump-induced Faraday rotation θ_{F} as a function of time t.

3.2. Single-pulse excitation

Figure 6(b) displays the experimental results: a harmonic oscillation with a period of 1 ps sets in within a single cycle, reaches its maximum amplitude at $t = 3$ ps, and decays exponentially with a time constant of 39 ps, thereafter. Coherent oscillations exceeding the noise floor may be resolved even after several hundreds of picoseconds (not shown). Figure 6(c) shows that the FT of the Faraday transient consists of a narrow peak at 1.0 THz, clearly identifying the signal as the magnetization signature of a coherent oscillation of a long-wavelength antiferromagnetic magnon in NiO. The spectrum of the Faraday signal also features a barely discernible faint peak at about 0.2 THz (figure 6(c)) that can be assigned to a lower-frequency long-wavelength magnon [51]. Our data do not show indications of broadband excitations such as Joule heating. Free-carrier and lattice absorption are also negligible because NiO is an insulator, and all optical phonon resonances are located above 12 THz, far beyond the frequencies considered here.

Most remarkably, the observed spin dynamics are driven by the magnetic field $\boldsymbol{B}$ only. Using a symmetry argument, the electric field $\boldsymbol{E}$ may safely be ruled out as an excitation channel: since the Faraday signal is proportional to the pump field [33], an electric dipole interaction with magnons (interaction energy $\propto \boldsymbol{M} \cdot \boldsymbol{E}$) would represent a linear magneto-electric effect. In centrosymmetric materials like NiO such processes are forbidden.

3.3. Microscopic description

In order to gain further insight into the spin motion and its driving force, we also performed microscopic simulations of the spin dynamics. As the driving THz transient has a wavelength that is large compared to the NiO lattice constant, spin motion is uniform within each $\langle 111 \rangle$ lattice plane. Thus, the magnetic state of NiO is adequately characterized by the spins $\boldsymbol{S}_1$ and $\boldsymbol{S}_2$ of adjacent $\langle 111 \rangle$ Ni^{2+} planes, and the spin Hamiltonian of [51] simplifies to

$$H = -J\boldsymbol{S}_1 \cdot \boldsymbol{S}_2 + \sum_{j=1}^{2} [D_x S_{jx}^2 + D_y S_{jy}^2] + \gamma \boldsymbol{B}(t) \cdot \sum_{j=1}^{2} \boldsymbol{S}_j. \tag{6}$$

Here, the first term describes the exchange interaction, and the exchange energy J is negative as the planes are antiferromagnetically coupled. The second term captures intrinsic anisotropic effects such as spin–spin magnetic–dipole coupling and the influence of the crystal potential on the spins mediated by the spin–orbit interaction. This anisotropy ensures that the spins are preferentially oriented in-plane along the $\langle 11\bar{2} \rangle$ direction. The last term describes the Zeeman interaction between the spins and the driving magnetic field. Considering $\boldsymbol{S}_1$ and $\boldsymbol{S}_2$ in equation (6) as classical observables, we obtain Landau–Lifshitz–Gilbert-type equations of spin motion,

$$\frac{\partial}{\partial t} \boldsymbol{S}_j = -\frac{\gamma}{1+\alpha^2} \left[\boldsymbol{S}_j \times \boldsymbol{B}_j^{\mathrm{eff}} - \frac{\alpha}{|\boldsymbol{S}_j|} \boldsymbol{S}_j \times (\boldsymbol{S}_j \times \boldsymbol{B}_j^{\mathrm{eff}}) \right], \tag{7}$$

where $\boldsymbol{B}_j^{\mathrm{eff}} = \boldsymbol{B}(t) - J\boldsymbol{S}_{3-j}/\gamma + (D_x S_{jx}, D_y S_{jy}, 0)^{\mathrm{t}}/\gamma$ is an effective magnetic field acting on spin j. Apart from the Gilbert damping constant α, which is adjusted to $(2.1 \pm 0.1) \times 10^{-4}$ to best replicate the measurement results, all parameters of equation (6) have been determined previously [51]. In particular, the driving field $\boldsymbol{B}$ is determined by taking the measured incident transient $B(t)$ (figure 6(a)) and accounting for multiple reflections at the NiO crystal surfaces.

By numerically solving equation (7) for $\boldsymbol{S}_1$ and $\boldsymbol{S}_2$, we obtain spin dynamics that are dominated by a precession with a period of 1 ps (figure 7(a)). S_{1y} exhibits an additional weak component with a period of about 5 ps, corresponding to the lower-frequency long-wavelength magnon of NiO at a frequency of ≈0.2 THz [51]. An image of the three-dimensional spin trajectory is displayed in figure 7(c): the Zeeman torque pulls the spins along the x-axis, thereby triggering a precessional motion about the equilibrium (z) direction. While the x component is antiparallel for both spins, the anisotropy field causes a smaller y component that leads to a non-vanishing macroscopic transient magnetization component M_y.

To arrive at the Faraday rotation, we use equation (5) and average $\boldsymbol{M} \propto \boldsymbol{S}_1 + \boldsymbol{S}_2$ over all S domains. Figure 6(b) demonstrates a striking agreement between experiment and theory, both with respect to the shape of the transient and its absolute magnitude. This result shows that the magnetic field of the incident THz pulse triggers a spin precession corresponding to the high-frequency long-wavelength magnon at 1 THz through the Zeeman interaction.

3.4. Coherent THz control of magnons by two-pulse excitation

The long lifetime of the spin precession (figure 6(b)) allows for it to be coherently controlled over quite a large time window. For this purpose, we excite the NiO with different sequences of two pulses. When the second THz pulse is applied precisely six precession cycles after the first, the amplitude of the induced magnetization doubles (figure 6(d)). This amplification arises because the torque of the second pulse is in phase with the spin precession induced by the first pulse. The amplification effect is reversed if the second pulse arrives 6.5 precession cycles after the first (figure 6(e)). In this case, the torque of the second pulse is entirely out of phase with the spin precession and switches the dynamics off. We note that our simulations again provide curves in excellent agreement with the experimental data.

3.5. Future directions: magnon probes and spin flips

We have successfully demonstrated the coherent control of ultrafast spin precession in antiferromagnetic NiO using the Zeeman torque of an intense THz transient. Such a control scheme is minimally invasive (as it leaves the non-spin degrees of freedom of the NiO in their ground state) and universal (as it is mediated by the Zeeman interaction). Coherent magnons may now be used as probes for ultrafast interactions of electron spin with orbital motion and lattice modes in essentially all THz-transparent matter and at all relevant frequencies.

We emphasize that Zeeman-driven spin motion is expected to be widely scalable, and our simulations based on equation (7) indicate a novel regime of dramatic THz nonlinearities beyond the perturbative regime. In contrast to the weak-field regime (figure 7(a)), THz peak amplitudes of 11 T lead to oscillations of S_{1x} significantly slower than the high-frequency magnon at 1 THz, and the evolution of S_{1y} is dominated by the low-frequency magnon at ≈0.2 THz (figure 7(b)). Note that both signals exhibit a modulation depth of nearly 100 %. Most remarkably, the change of S_{1z} from 1 to nearly -1 demonstrates the induction of a spin flip, which also becomes apparent in an image of the three-dimensional spin trajectory (figure 7(d)). It is not obvious whether in such an extreme excitation regime the parameters of the spin Hamiltonian of equation (6) can still be assumed to be constant. However, recent modeling based on an extended Hamiltonian has demonstrated similar magnetization dynamics [52]. In any case, future studies of high-field-driven THz spin dynamics will enter an entirely new territory of many-body physics.

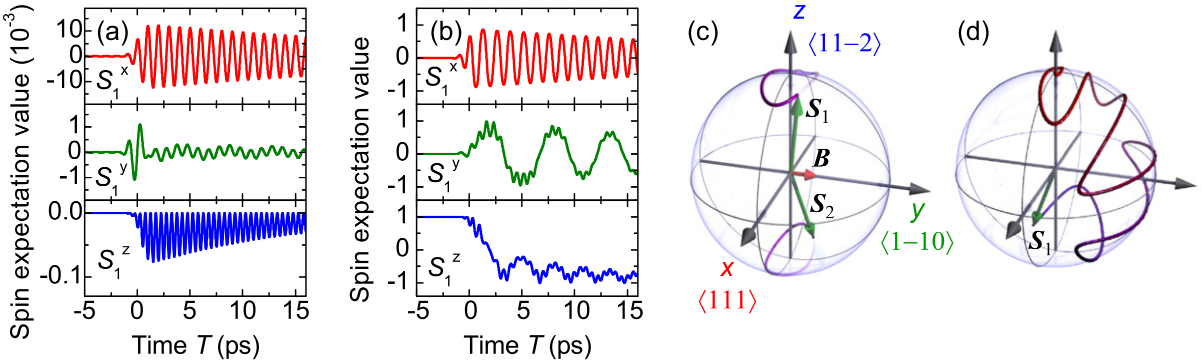

Figure 7. Simulated dynamics of sublattice spin $\boldsymbol{S}_1$ (a) under the excitation conditions used in the experiment (peak driving field 0.14 T) and (b) with a peak field of 11 T. (c, d) Three-dimensional spin trajectories resulting from (a) and (b), respectively. In (c), spin deflections are numerically enhanced for better visibility.

4. Conclusions and perspectives

Intense electric and magnetic multi-THz fields have become versatile tools to selectively and coherently control electronic or spin degrees of freedom of condensed matter in a previously elusive spectral range, and in the sub-optical-cycle temporal regime. Our study of multi-THz two-dimensional spectroscopy confirms the onset of a non-perturbative response under even off-resonant excitation of interband transitions in InSb. Peak electric fields above 5 MV cm^{-1} lead to carrier-wave Rabi flopping between the valence and conduction bands. These results underpin the large potential of novel strong-field multi-THz technology for high harmonics generation [53] and coherent quantum control of low-energy excitations [22, 54]. The unique capability of field-sensitive multi-dimensional spectroscopy to separate purely coherent and incoherent nonlinearities may open a new chapter in the investigation of collective low-energy excitations including inter-molecular vibrations in hydrogen-bonded liquids [55] and Cooper pair breaking transitions in superconductors [56]. On the other hand, all-magnetic spin control opens the door to the new concept of THz electron spin resonance. Coherent magnons in systems as diverse as ferro- and antiferromagnets or high-temperature superconductors may, for instance, be employed as unique probes of ultrafast interactions with lattice and charge degrees of freedom. Furthermore, our experiments may inspire the development of ultrafast next-generation memory devices, spin-based quantum computation and spintronics. This is only the beginning of a new era of sub-cycle multi-THz coherent control of condensed matter.

Acknowledgments

We thank A Leitenstorfer, M Wolf, M Fiebig, B Mayer, O Schubert, F Junginger, S Mährlein, C Schmidt, G Klatt and T Dekorsy for ongoing collaborations which laid the basis for this work. We also appreciate fruitful discussions with T Cocker, D Seletskiy, M P Hasselbeck and M Sheik-Bahae. Financial support by Deutsche Forschungsgemeinschaft (DFG) through projects PA 2113/1-1 and HU 1598/1-1 as well as by the European Research Council via ERC Starting Grant QUANTUMsubCYCLE is gratefully acknowledged.

References

[1] Tonouchi M 2007 Cutting-edge terahertz technology *Nature Photon.* **1** 97–105

[2] Ulbricht R, Hendry E, Shan J, Heinz T F and Bonn M 2011 Carrier dynamics in semiconductors studied with time-resolved terahertz spectroscopy *Rev. Mod. Phys.* **83** 543–86

[3] Sell A, Scheu R, Leitenstorfer A and Huber R 2008 Field-resolved detection of phase-locked infrared transients from a compact Er:fiber system tunable between 55 and 107 THz *Appl. Phys. Lett.* **93** 251107

[4] Ashida M 2008 Ultra-broadband terahertz wave detection using photoconductive antenna *Japan J. Appl. Phys.* **47** 8221–5

[5] Günter G, Anappara A A, Hees J, Sell A, Biasiol G, Sorba L, De Liberato S, Ciuti C, Tredicucci A, Leitenstorfer A and Huber R 2009 Sub-cycle switch-on of ultrastrong light–matter interaction *Nature* **458** 178–81

[6] Bartel T, Gaal P, Reimann K, Woerner M and Elsaesser T 2005 Generation of single-cycle THz transients with high electric-field amplitudes *Opt. Lett.* **30** 2805–7

[7] Blanchard F *et al* 2011 Generation of intense terahertz radiation via optical methods *IEEE J. Sel. Topics Quantum Electron.* **17** 5–16

[8] Hebling J, Yeh K-L, Hoffmann M C, Bartal B and Nelson K A 2008 Generation of high-power terahertz pulses by tilted-pulse-front excitation and their application possibilities *J. Opt. Soc. Am.* B **25** B6–19

[9] Hirori H, Doi A, Blanchard F and Tanaka K 2011 Single-cycle terahertz pulses with amplitudes exceeding 1 MV cm^{-1} generated by optical rectification in LiNbO$_3$ *Appl. Phys. Lett.* **98** 091106

[10] Minami Y, Kurihara T, Yamaguchi K, Nakajima M and Suemoto T 2013 High-power THz wave generation in plasma induced by polarization adjusted two-color laser pulses *Appl. Phys. Lett.* **102** 041105

[11] Razzari L *et al* 2009 Nonlinear ultrafast modulation of the optical absorption of intense few-cycle terahertz pulses in n-doped semiconductors *Phys. Rev.* B **79** 193204

[12] Su F H *et al* 2009 Terahertz pulse induced intervalley scattering in photoexcited GaAs *Opt. Express* **17** 9620–9

[13] Turchinovich D, Hvam J M and Hoffmann M C 2012 Self-phase modulation of a single-cycle terahertz pulse by nonlinear free-carrier response in a semiconductor *Phys. Rev.* B **85** 201304

[14] Kuehn W, Gaal P, Reimann K, Woerner M, Elsaesser T and Hey R 2010 Terahertz-induced interband tunneling of electrons in GaAs *Phys. Rev.* B **82** 075204

[15] Hoffmann M C, Hebling J, Hwang H Y, Yeh K-L and Nelson K A 2009 Impact ionization in InSb probed by terahertz pump—terahertz probe spectroscopy *Phys. Rev.* B **79** 161201

[16] Hirori H, Shinokita K, Shirai M, Tani S, Kadoya Y and Tanaka K 2011 Extraordinary carrier multiplication gated by a picosecond electric field pulse *Nature Commun.* **2** 594

[17] Blanchard F *et al* 2011 Effective mass anisotropy of hot electrons in nonparabolic conduction bands of n-doped InGaAs films using ultrafast terahertz pump–probe techniques *Phys. Rev. Lett.* **107** 107401

[18] Katayama I, Aoki H, Takeda J, Shimosato H, Ashida M, Kinjo R, Kawayama I, Tonouchi M, Nagai M and Tanaka K 2012 Ferroelectric soft mode in a SrTiO$_3$ thin film impulsively driven to the anharmonic regime using intense picosecond terahertz pulses *Phys. Rev. Lett.* **108** 097401

[19] Rini M, Tobey R, Dean N, Itatani J, Tomioka Y, Tokura Y, Schoenlein R W and Cavalleri A 2007 Control of the electronic phase of a manganite by mode-selective vibrational excitation *Nature* **449** 72–4

[20] Dienst A, Hoffmann M C, Fausti D, Petersen J C, Pyon S, Takayama T, Takagi H and Cavalleri A 2011 Bi-directional ultrafast electric-field gating of interlayer charge transport in a cuprate superconductor *Nature Photon.* **5** 485–8

[21] Luo C W, Reimann K, Woerner M, Elsaesser T, Hey R and Ploog K H 2004 Phase-resolved nonlinear response of a two-dimensional electron gas under femtosecond intersubband excitation *Phys. Rev. Lett.* **92** 047402

[22] Leinß S, Kampfrath T, Volkmann K v., Wolf M, Steiner J T, Kira M, Koch S W, Leitenstorfer A and Huber R 2008 Terahertz coherent control of optically dark paraexcitons in Cu$_2$O *Phys. Rev. Lett.* **101** 246401

[23] Kuehn W, Gaal P, Reimann K, Woerner M, Elsaesser T and Hey R 2010 Coherent ballistic motion of electrons in a periodic potential *Phys. Rev. Lett.* **104** 146602

[24] Zaks B, Liu R B and Sherwin M S 2012 Experimental observation of electron-hole recollisions *Nature* **483** 580–3

[25] Fleischer S, Zhou Y, Field R W and Nelson K A 2011 Molecular orientation and alignment by intense single-cycle THz pulses *Phys. Rev. Lett.* **107** 163603

[26] Fleischer S, Field R W and Nelson K A 2012 Commensurate two-quantum coherences induced by time-delayed THz fields *Phys. Rev. Lett.* **109** 123603

[27] Sell A, Leitenstorfer A and Huber R 2008 Phase-locked generation and field-resolved detection of widely tunable terahertz pulses with amplitudes exceeding 100 MV cm^{-1} *Opt. Lett.* **33** 2767–9

[28] Junginger F, Sell A, Schubert O, Mayer B, Brida D, Marangoni M, Cerullo G, Leitenstorfer A and Huber R 2010 Single-cycle multiterahertz transients with peak fields above 10 MV cm^{-1} *Opt. Lett.* **35** 2645–7

[29] Wegener M 2004 *Extreme Nonlinear Optics* 1st edn (Berlin: Springer)

[30] Yamaguchi K, Nakajima M and Suemoto T 2010 Coherent control of spin precession motion with impulsive magnetic fields of half-cycle terahertz radiation *Phys. Rev. Lett.* **105** 237201

[31] Zhou R, Jin Z, Li G, Ma G, Cheng Z and Wang X 2012 Terahertz magnetic field induced coherent spin precession in $\mathrm{YFeO_3}$ *Appl. Phys. Lett.* **100** 061102

[32] Junginger F, Mayer B, Schmidt C, Schubert O, Mährlein S, Leitenstorfer A, Huber R and Pashkin A 2012 Nonperturbative interband response of a bulk InSb semiconductor driven off resonantly by terahertz electromagnetic few-cycle pulses *Phys. Rev. Lett.* **109** 147403

[33] Kampfrath T, Sell A, Klatt G, Pashkin A, Ma S, Dekorsy T, Wolf M, Fiebig M, Leitenstorfer A and Huber R 2011 Coherent terahertz control of antiferromagnetic spin waves *Nature Photon.* **5** 31–4

[34] Hebling J, Hoffmann H C, Hwang H Y, Yeh K-L and Nelson K A 2010 Observation of nonequilibrium carrier distribution in Ge, Si and GaAs by terahertz pump— terahertz probe measurements *Phys. Rev.* B **81** 035201

[35] Kuehn W, Reimann K, Woerner M and Elsaesser T 2009 Phase-resolved two-dimensional spectroscopy based on collinear n-wave mixing in the ultrafast time domain *J. Chem. Phys.* **130** 164503

[36] Olszak P D, Cirloganu C M, Webster S, Padilha L A, Guha S, Gonzalez L P, Krishnamurthy S, Hagan D J and van Stryland E W 2010 Spectral and temperature dependence of two-photon and free-carrier absorption in InSb *Phys. Rev.* B **82** 235207

[37] Sheik-Bahae M, Rossi T and Kwok H S 1987 Frequency dependence of the two-photon absorption coefficient in InSb: tunneling effects *J. Opt. Soc. Am.* B **4** 1964–9

[38] Yuen S Y and Wolff P A 1982 Difference-frequency variation of the free-carrier-induced, third-order nonlinear susceptibility in n-InSb *Appl. Phys. Lett.* **40** 457–9

[39] Hutchings D C, Sheik-Bahae M, Hagan D J and van Stryland E W 1992 Kramers-Kronig relations in nonlinear optics *Opt. Quantum Electron.* **24** 1–30

[40] Ziolkowski R W, Arnold J M and Gogny D M 1995 Ultrafast pulse interactions with two-level atoms *Phys. Rev.* A **52** 3082–94

[41] Thomas Andrews J and Sen P 1998 Effect of non-centrosymmetry on stark broadening in bulk indium antimonide crystal *Quantum Semiclass. Opt.* **10** 663

[42] Mücke O D, Tritschler T, Wegener M, Morgner U and Kärtner F X 2001 Signatures of carrier-wave rabi flopping in GaAs *Phys. Rev. Lett.* **87** 057401

[43] Tritschler T, Mücke O D and Wegener M 2003 Extreme nonlinear optics of two-level systems *Phys. Rev.* A **68** 033404

[44] Ghimire S, DiChiara A D, Sistrunk E, Agostini P, DiMauro L F and Reis D A 2011 Observation of high-order harmonic generation in a bulk crystal *Nature Phys.* **7** 138–41

[45] Merlin R 2009 Metamaterials and the Landau-Lifshitz permeability argument: large permittivity begets high-frequency magnetism *Proc. Natl Acad. Sci. U.S.A.* **106** 1693–8

[46] Hiebert W K, Stankiewicz A and Freeman M R 1997 Direct observation of magnetic relaxation in a small permalloy disk by time-resolved scanning kerr microscopy *Phys. Rev. Lett.* **79** 1134–7

[47] Back C H, Allenspach R, Weber W, Parkin S S P, Weller D, Garwin E L and Siegmann H C 1999 Minimum field strength in precessional magnetization reversal *Science* **285** 864–7

[48] Wang Z, Pietz M, Walowski J, Förster A, Lepsa M I and Münzenberg M 2008 Spin dynamics triggered by subterahertz magnetic field pulses *J. Appl. Phys.* **103** 123905

[49] Kirilyuk A, Kimel A V and Rasing T 2010 Ultrafast optical manipulation of magnetic order *Rev. Mod. Phys.* **82** 2731–84

[50] Sänger I, Pavlov V V, Bayer M and Fiebig M 2006 Distribution of antiferromagnetic spin and twin domains in NiO *Phys. Rev.* B **74** 144401

[51] Hutchings M T and Samuelsen E J 1972 Measurement of spin-wave dispersion in NiO by inelastic neutron scattering and its relation to magnetic properties *Phys. Rev.* B **6** 3447–61

[52] Wienholdt S, Hinzke D and Nowak U 2012 THz switching of antiferromagnets and ferrimagnets *Phys. Rev. Lett.* **108** 247207

[53] Golde D, Meier T and Koch S W 2008 High harmonics generated in semiconductor nanostructures by the coupled dynamics of optical inter- and intraband excitations *Phys. Rev.* B **77** 075330

[54] Cole B E, Williams J B, King B T, Sherwin M S and Stanley C R 2001 Coherent manipulation of semiconductor quantum bits with terahertz radiation *Nature* **410** 60–3

[55] Cowan M L, Bruner B D, Huse N, Dwyer J R, Chugh B, Nibbering E T J, Elsaesser T and Miller R J D 2005 Ultrafast memory loss and energy redistribution in the hydrogen bond network of liquid H_2O *Nature* **434** 199–202

[56] Papenkort T, Kuhn T and Axt V M 2008 Coherent control of the gap dynamics of BCS superconductors in the nonadiabatic regime *Phys. Rev.* B **78** 132505